



# Development of a Single-Sided Magnetic Resonance Surface Scanner: Towards Non-Destructive Quantification of Moisture in Slaked Lime Plaster for Maintenance and Remediation of Heritage Architecture

Yoshito Nakashima<sup>1</sup>

Received: 15 October 2022 / Accepted: 28 August 2023 / Published online: 26 September 2023  
© The Author(s) 2023

## Abstract

Single-sided time-domain proton magnetic resonance (MR) surface scanners are useful for non-destructive measurements of moisture. A mobile single-sided MR sensor unit employing two concentric ring magnets was constructed for the in situ quantification of moisture in slaked lime plaster used in the outer walls and roofs of heritage architecture. This sensor unit allows for non-destructive measurements of water proton relaxation 1.5 to 13.5 mm beneath the surfaces of walls and roofs. The following laboratory experiments on water-saturated porous slaked lime plaster samples were performed. (i) The porosity (water volume fraction) was measured in approximately eight minutes with a root mean square error of 1.9 vol%. (ii) The fundamental MR-related property (i.e. proton surface relaxivity) needed for the estimation of the pore size distribution was also measured successfully. (iii) The pore volume expansion due to frost damage was successfully detected as a significant change in the transverse relaxation time distribution. These results demonstrate that the portable MR surface scanner is a promising non-destructive testing tool for the maintenance and remediation of heritage architecture made of plaster.

**Keywords** Freeze–thawing · Plaster · Proton nuclear magnetic resonance · Single-sided magnetic resonance scanner · Water

## 1 Introduction

A single-sided low-field time-domain magnetic resonance (MR) surface scanner is a useful measurement tool that uses proton relaxometry [1–3]. Due to the carefully designed magnetic circuit and pulse sequence [4–11], it enables non-destructive, non-invasive, and non-contact scans of the surfaces of large objects. The scanner system is portable and lightweight owing to its construction with compact rare-earth permanent magnets, and has an investigation depth of several millimeters to several centimeters. MR surface scanners are now being applied in a diverse range of fields for the in situ non-destructive moisture measurements [1–3, 12–14].

Although the quantum physics-based principle of proton MR is complicated and the single-sided MR scanner system is expensive, MR scanning has the following advantages with respect to the in situ non-destructive moisture

quantification. (a) The sensed region is compact (typically,  $\approx 1 \times 1 \times 1 \text{ cm}^3$ ) and its location is accurately known [2, 10]. (b) The pore size distribution and the permeability of water-filled porous media can be estimated [11, 15]. (c) The depth-profiling or one-dimensional imaging of the water distribution at a spatial resolution of tens to hundreds of micrometers is possible [16, 17]. (d) The mobility of water molecules (i.e. restricted diffusion of pore water molecules) can be measured [1, 2]. (e) Non-contact scanning is also possible, which would be essential for the inspection of world heritage walls with priceless paintings [18–20]. It should be noted that other non-destructive methods for the in situ moisture quantification of building materials (i.e. near-infrared spectroscopy, infrared thermography, electrical resistance and capacitance, self-potential, evanescent-field dielectrometry, time-domain reflectometry, ground penetrating radar, terahertz waves, light detection and ranging scanning, and ultrasonic methods [21–27]) could not meet the above mentioned five features, (a) to (e), simultaneously.

The present study focuses on the application of a single-sided MR surface scanner to the non-destructive measurement of moisture in slaked lime plaster for the maintenance and remediation of heritage architecture. Slaked lime plaster

✉ Yoshito Nakashima  
nakashima.yoshito@aist.go.jp

<sup>1</sup> National Institute of Advanced Industrial Science and Technology (AIST), Central 7, 1-1-1 Higashi, Tsukuba, Ibaraki 305-8567, Japan

powder is one of most typical geomaterials used for construction, and mainly consists of calcium hydroxide,  $\text{Ca}(\text{OH})_2$  [28–30]. It is kneaded with water to cover surfaces of walls and fill gaps in roofs in heritage architecture [31–34]. The calcium hydroxide reacts with the atmospheric carbon dioxide to form calcite, which causes mechanical hardening of the plaster [28–30, 33]. The moisture in the porous plaster is a key aspect of the material because water-filled pores inhibit the reaction of calcium hydroxide grains with atmospheric carbon dioxide [33], resulting in delayed hardening. Moisture also plays an important role in frost damage in cold regions [35–38]. When freezing, the water volume increases by approximately 9% [39]. This freezing-driven volume increase of pore water could expand or destroy the solid framework of building materials such as slaked lime plaster. The resultant bulk volume expansion or cracking [38] could reduce the mechanical strength of the architecture. Non-destructive moisture scanning is therefore essential for the maintenance and remediation of the walls and roofs of priceless world heritage architecture and national treasures, and single-sided MR surface scanners are suitable for this purpose.

Single-sided MR surface scanners have been applied to heritage architecture made of various types of plaster (slaked lime, cement, and gypsum), natural stones, and bricks [16–20, 40–47]. In the present study, the following three aspects are integrated from previous single-sided MR scanning studies on heritage architecture:

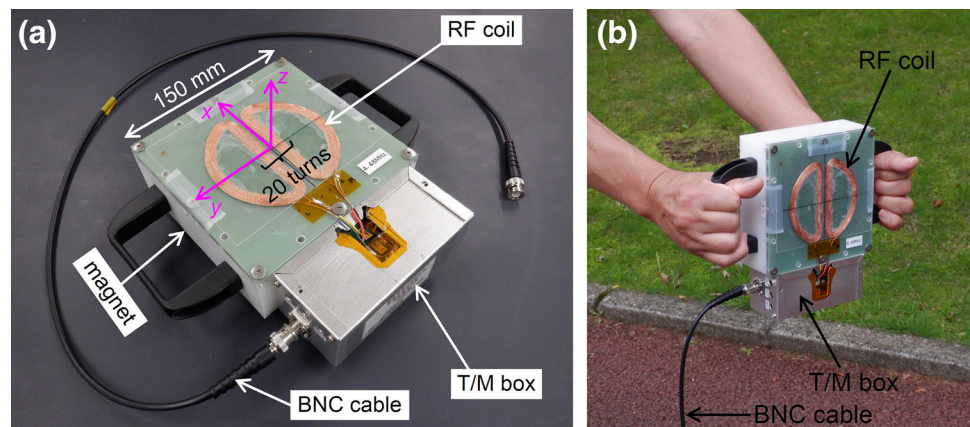
- (i) The applicability of single-sided MR scanning to the evaluation of frost damage [35–37], which is critical for the conservation of heritage architecture made of plaster in the cold regions, was examined for the first time. The pore size can increase when liquid water in pores is frozen into ice and expands. A time-domain MR scanner enables measurement of the proton transverse relaxation time ( $T_2$ ) of pore water, which could be converted into the pore size distribution [15] for porous plaster samples. Frost damage to cultural heritage was simulated in the laboratory by freeze–thawing of water-saturated plaster samples, and the increase in pore size after freeze–thawing was measured by analyzing the change in the transverse relaxation time.
- (ii) To the best of our knowledge, there are few reports on the fundamental MR-related properties of slaked lime plaster. Thus, measurements of the pore structure, longitudinal relaxation time ( $T_1$ ), and  $T_1$ - and  $T_2$ -proton surface relaxivities ( $\rho_1$  and  $\rho_2$ , respectively) [15] were performed for the first time in the laboratory. The measured  $\rho_2$  value was applied to the analysis of the pore size distribution in (i).
- (iii) In previous single-sided MR studies pertaining to heritage architecture [16–20, 40–47], the dimensions of the sensed region of the mobile MR sensor unit were small (e.g.  $\approx 100 \text{ mm}^2$  parallel to the sensor face,  $\approx 2 \text{ mm}$  normal to the sensor face) [43]. This is a consequence of the magnetic circuit with a strong field gradient. While the small dimension normal to the sensor surface allows for high-resolution depth profiling [19, 20, 40], it is not adequate for determining the gross moisture content of the walls and roofs, as they have strong heterogeneity inside the plaster (e.g. large voids). Thus, in the present study, a different type of a magnetic circuit with a homogeneous magnetic field (i.e. a sweet spot) [1, 2, 5, 6, 10, 48, 49] was employed, which enlarges the sensed region. One of the recent progresses in the magnetic circuit design with a sweet spot is the use of two concentric ring magnets [50]. The interaction of each ring magnet significantly increases the volume of the sensed region. We optimized the dimensions of the two concentric ring magnets by computer simulations, and constructed the magnetic circuit using Nd–Fe–B permanent magnets. As a result, the dimensions of the sensed region are as large as  $304 \text{ mm}^2$  parallel to and  $12 \text{ mm}$  normal to the sensor face, which are sufficient to measure the gross moisture content of the subsurface of wet plaster walls and roofs. The MR surface scanner equipped with the developed magnetic circuit was used for the investigation of the items (i) and (ii) above. The accuracy of the water volume fraction (i.e. porosity) for intact plaster samples was also examined to evaluate the basic performance of the MR scanner as a moisture quantification tool.

## 2 Methods and Materials

### 2.1 Single-Sided MR Sensor Unit

The mobile MR sensor unit constructed in the present study is shown in Fig. 1. It consists of a single-sided permanent magnetic circuit with handles and a double D-shaped planar radio-frequency (RF) coil with an aluminum tuning/matching (T/M) box. During operation, the RF coil is connected to an MR console via a BNC cable. The total weight of the sensor unit is 4.3 kg without the BNC cable. Due to the single-sided magnet geometry, one side of the planar RF coil is exposed to free space (i.e.  $z > 0$  in Fig. 1a), which allows for non-destructive scanning of the surfaces of large objects.

**Fig. 1** Sensor unit constructed for the single-sided MR surface scanner system. **a** Photograph of sensor unit with the scanning surface facing upward. The origin of the Cartesian  $x$ - $y$ - $z$  coordinate system is marked on the PMMA plate. The origin of the  $x$ - $y$  coordinate system is centered at the RF coil, and thus the  $z$ -axis coincides with the cylindrical magnet axis. **b** Snapshot of the mobile sensor unit. A photograph without the RF coil is shown in Fig. ESM2a



A double D-shaped RF coil [50] was employed for the excitation of nuclear spins and detection of the resultant proton relaxation (Fig. 1). This double D-shaped (not solenoidal) design is essential for producing an RF magnetic field oscillating normal to the direction of the static magnetic field in the sensed region. Using this design, the RF magnetic field is in the  $y$ -direction while the static field is in the  $z$ -direction in Fig. 1a. The details of the RF circuit are also schematically shown in Fig. ESM1 in Electronic Supplementary Material. Larmor frequency tuning and  $50 \Omega$  matching were performed using non-magnetic trimmer capacitors in the T/M box. A transparent poly methyl methacrylate (PMMA) plate ( $14 \times 11 \text{ mm}^2$ , 1 mm thick) was placed on the RF coil (Fig. 1) to mechanically protect the coil and to electromagnetically decouple the coil from samples with various impedance values.

Nd-Fe-B permanent magnets (NEOMAX®, Hitachi Metals, Ltd., Tokyo, Japan) were employed for the magnetic material in the present study. The residual flux density of the magnet was  $\approx 1.4 \text{ T}$ , and the coercivity was  $\approx 1.1 \text{ MA/m}$ . The geometry of the magnetic circuit was optimally determined by numerical simulations as follows [51]. Briefly, two concentric ring magnets whose end faces were polarized [50, 52], were considered. There was a recess between the end surfaces of the inner ring magnet and the outer ring magnet in order to produce a sweet spot in the sensed region. Extensive static magnetic field simulations were performed for various values of the diameter, thickness, length of the ring magnets and the recess with the constraint of that the total magnet weight remains constant. Approximately 1.3 million cases were examined to search for the best geometry, which should produce a strong and broad sweet spot far from the end surface of the outer ring magnet. As a result, the magnetic circuit shown in Fig. ESM2a was chosen [51], for which the spatial distribution of the magnetic field measured by a Tesla meter is shown in Fig. ESM2b.

Although the exact shape of the sensed region of the single-sided MR sensor is generally rather irregular [10, 48,

50], we approximate this shape to be a simple cuboid [49] in the present study. The dimensions and location of this cuboid region were measured using silicon rubber sheets. The detailed procedure for these measurements is described elsewhere [49, 50, 53]. The duration of the  $90^\circ$  and  $180^\circ$  RF pulses employed in the silicon rubber experiments was 0.06 ms. The obtained sensitivity profile with the static magnetic field distribution in the  $z$ -direction is shown in Fig. 2, and those for the  $x$ - and  $y$ -directions are shown in Fig. ESM3. Based on the measurements, the investigation depth was determined to be 6 mm (Fig. 2); the sensed region almost agreed with the region with the homogeneous static magnetic field (i.e. sweet spot) in Fig. ESM2b, and the dimensions of this sensed region when approximated as a cuboid were 19, 16, and 12 mm along the  $x$ -,  $y$ -, and  $z$ -axes, respectively. The sensed region in the  $z$ -direction ranges from  $z = 1.5$  to 13.5 mm (width, 12 mm), which is sufficient to measure the gross moisture content of the plaster walls of the world heritage architecture as thick as a few centimeters [54].

In comparison, the dimensions of the sensed region along the  $x$ -,  $y$ -, and  $z$ -axes of the single-sided MR scanner used in previous studied on heritage architecture were 30, 30, and 0.2 mm, respectively [42]. The moisture level in such a small sensed region could strongly fluctuate if by chance an unusual feature is detected (e.g. large water-filled voids or large gravel inclusions); these are occasionally embedded in the region to be scanned. The very large ratio between the scanned region volume in the present study and in the previous studies ( $19 \times 16 \times 12 / (30 \times 30 \times 0.2) \approx 20$ ) shows that the moisture data acquired using the MR scanner in the present study provides a more reliable average moisture value for the heterogeneous plaster found in heritage architecture.

The total volume of  $19 \times 16 \times 12 \approx 3650 \text{ mm}^3$  was achieved using the two concentric ring magnets (Fig. ESM2) weighing a total of 2.7 kg. In contrast, the sensed region of the sweet-spot type magnetic circuit (a ring magnet and a bar magnet) for the same Larmor frequency of 4.5 MHz in a previous study [55] was  $14 \times 15 \times 11 = 2310 \text{ mm}^3$  using

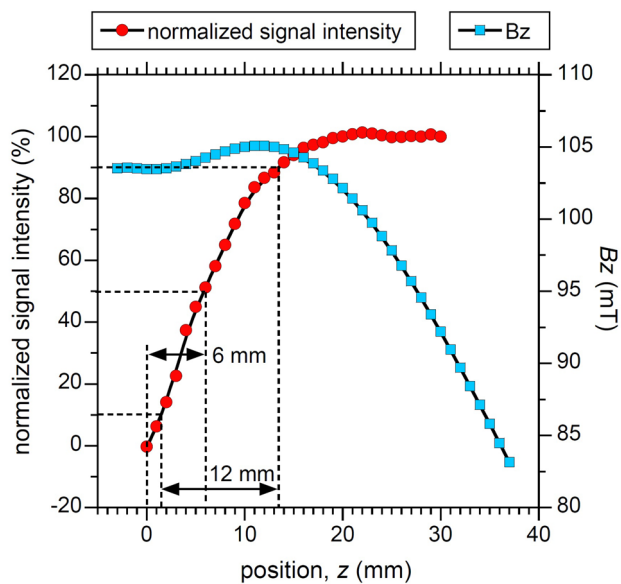


**Fig. 2** Sensitivity distribution along the  $z$ -direction determined by measuring MR signal intensity dependence on the thickness of stacked silicon rubber sheets (dimensions,  $30 \times 30 \times 1$  mm for each). All solid lines are for eye-guiding. First, 30 stacked sheets were placed on the center of the sensor to completely encompass the sensed region. Then, the NMR signal intensity was measured based on the summation of echoes using the CPMG sequence. The rubber sheets were removed sheet by sheet, starting from the top (i.e.  $z = 30$  mm) to measure the MR signal intensity decrease that occurred as the number of the stacked sheets decreased. The obtained summation of echoes was normalized and plotted against the thickness of the rubber sheets (the horizontal axis is the position of the removal front of the stacked sheets). The distribution of the  $z$ -component ( $B_z$ ) of the magnetic flux density vector along the  $z$ -axis (i.e.  $x = y = 0$  mm) measured by the Hall probe was superimposed, which was taken from Fig. ESM2b. According to the previous studies [49, 53], it was tentatively assumed that normalized signal intensities of 10, 90, and 50% correspond to the lower and upper limits of the sensed region and the investigation depth of the sensor, respectively. As a result, the width of the sensed region was determined to be 12 mm in the  $z$ -direction, and the investigation depth was 6 mm from the PMMA plate on the planar coil. The sensitivity distributions along the  $x$ - and  $y$ -directions are shown in Fig. ESM3

Nd–Fe–B magnets weighing a total of 3.4 kg, heavier than 2.7 kg. This weight comparison demonstrates the advantage of the concept of the two concentric ring magnets [50] over the conventional sweet-spot type magnet design. The volume of the sensed region in the present study was increased by  $3650/2310 \approx 1.6$  times, which would ensure MR signals with better signal-to-noise ratios.

## 2.2 Sample Description

A powder product of slaked lime plaster manufactured by Tokyo Sun-Home Co. Ltd. (Tokyo, Japan) was used in the present study. The main component is portlandite,  $\text{Ca}(\text{OH})_2$ . Plant fiber and binder are included as minor components. The chemical composition of the powder as oxides obtained by

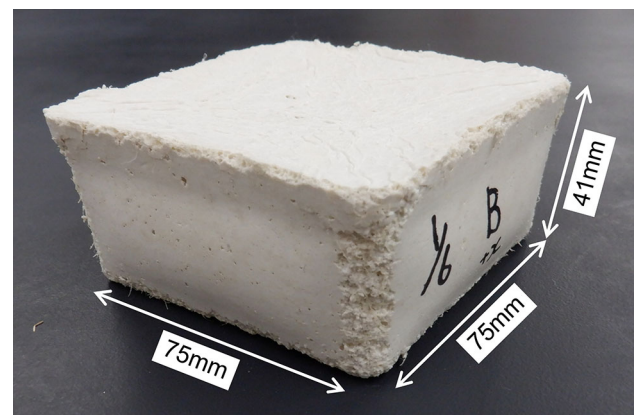


**Fig. 3** Photograph of a slaked lime plaster sample (sample B listed in Table ESM2) measured by the MR surface scanner

X-ray fluorescence analysis with the fundamental parameter method was:  $\text{SiO}_2$ , 0.25;  $\text{Fe}_2\text{O}_3$ , 0.07;  $\text{CaO}$ , 75.57;  $\text{P}_2\text{O}_5$ , 0.03;  $\text{SrO}$ , 0.05;  $\text{SO}_3$ , 0.11; and loss on ignition (e.g.  $\text{H}_2\text{O}$  and  $\text{CO}_2$ ), 23.92 (total 100 wt%). The powder was kneaded with tap water followed by curing in containers made of silicon rubber. The solidified plaster samples were taken out of the containers after curing. The plaster samples were dried at  $50^\circ\text{C}$  in an oven without the function of the humidity control to measure the dry weight (approximately 300 g), and then saturated with tap water to measure the water-saturated weight (approximately 400 g). A photograph of a slaked lime plaster sample prepared is shown in Fig. 3. The dry-wet weight difference method allows for the calculation of the ground truth value of the porosity (i.e. water volume fraction of the water-saturated sample) to evaluate the measurement accuracy by MR scanning. It should be noted that this weight-difference method using relatively large samples is better than the mercury porosimetry using small samples (approximately 0.5 g). This is because the large sample volume reduces the statistical fluctuation due to the intrinsic spatial heterogeneity of the pore structure of the plaster samples, ensuring the better accuracy for the porosity values. Detailed data on the slaked lime plaster samples prepared in the present study are listed in Tables ESM1 and ESM2.

The physical and chemical properties of the plaster samples were measured for use as references for the MR experiments. The pore structure is an especially important property because the proton relaxation times ( $T_1$  and  $T_2$ ) for pore water are sensitive to the pore size distribution [15, 56]. For pores ranging from 10 nm to  $100\ \mu\text{m}$  in diameter, the pore size distribution was obtained by mercury porosimetry (Fig. 4 and Table ESM1). No significant difference in the pore size distribution and the surface-to-volume ratio for the pores was observed among the three intact samples with different water fractions used during the kneading step. Thus, all plaster samples for MR measurements and X-ray computed tomography



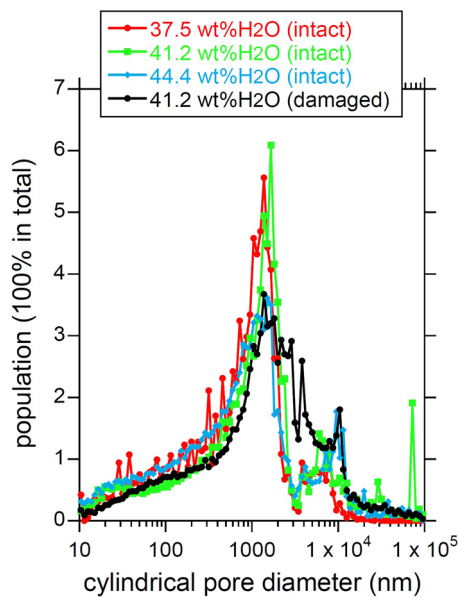


**Fig. 4** Pore size distribution for slaked lime plaster samples obtained by mercury porosimetry for three intact samples kneaded with different water fractions. Data for a plaster sample damaged by freeze–thaw processing are also superimposed. See Table ESM1 for the detailed data

(CT) were kneaded with water at a fixed value of 41.2 wt% H<sub>2</sub>O (see Table ESM2). It should be noted that the water content, 41.2 wt% H<sub>2</sub>O, is typical for the heritage architecture [32]. For pores larger than a few hundred micrometers, X-ray tomography was applied. Dry porous plaster samples were imaged by X-ray CT at three different spatial resolutions (Fig. ESM4a–c), and all depicted a number of subspherical voids probably produced during the kneading process. The mineral composition of the plaster sample was analyzed by X-ray powder diffractometry (Fig. ESM4d). The results show that the main components are portlandite, Ca(OH)<sub>2</sub>, and calcite, CaCO<sub>3</sub>, which agrees with the literature [29, 30]. The freezing temperature of the pore water was determined by measuring the intensity of the proton free induction decay (FID) signal derived from the liquid water. Details on the FID method are described elsewhere [57]. The results in Fig. ESM4e show that almost all of the pore water (i.e. 91%) freezes at  $-6\text{ }^{\circ}\text{C}$ . This is consistent with reports that the freezing point of pore water in porous media with pore sizes of sub-micrometers is often beneath  $0\text{ }^{\circ}\text{C}$  [57, 58].

### 2.3 MR Scanning of Plaster Samples

All single-sided MR experiments were performed using a portable MR console system (MRTechnology Inc., Tsukuba, Japan) [59] equipped with the developed sensor unit (Fig. 1). The proton Larmor frequency corresponding to the magnetic flux density in the sensed region (Figs. 2 and ESM2b and

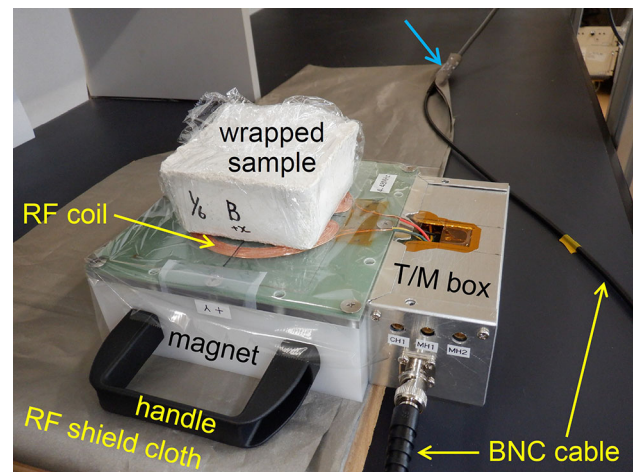


**Fig. 5** Measurement setup for MR surface scanning of the water-saturated plaster sample B in Fig. 3. A wide-angle photograph of this scene is shown in Fig. ESM5. The plaster sample is placed on the center (i.e.  $x = y = 0$ ) of the RF coil shown in Fig. 1

ESM3) was 4.5 MHz within a room temperature range of  $26 \pm 2\text{ }^{\circ}\text{C}$ . A snapshot of a plaster sample measurement is shown in Figs. 5 and ESM5. The RF shield cloth provides an electric ground via connection to the outer shield of the BNC cable at the position indicated by the blue arrow in Fig. 5 (see also the blue mark in Fig. ESM1). The T/M operations were performed with the capacitors shown in Fig. ESM1 using a Smith chart [2] displayed on a network analyzer, and then the transient proton relaxation was measured. The resultant quality factor  $Q$  for the RF coil after the T/M adjustment was almost independent of the samples and constant ( $\approx 31$ ), partly due to the PMMA plate placed on the RF coil to electromagnetically decouple the coil from the sample.

A phase-alternated pair-stacking (PAPS) Carr–Purcell–Meiboom–Gill (CPMG) pulse sequence [11] was employed to acquire the proton transverse relaxation data. The parameters for the CPMG sequence were as follows. The duration of the  $90^{\circ}$  and  $180^{\circ}$  RF pulses was 0.06 ms, the echo spacing was 0.5 ms, the sequence repetition time,  $TR$ , was 5 s (i.e. the  $T_1$  full relaxation condition), and the number of echoes acquired was approximately 1000. For the number of stacked signals,  $N_{\text{stack}}$ , five values (6, 12, 24, 48, and 96) were employed to evaluate its effect on the measurement accuracy. The number of dummy scans without the CPMG train data acquisition was unity. Thus, for example, the required MR measurement time for each sample was  $5\text{ s} \times (6 + 1)\text{ times} = 35\text{ s}$  for  $N_{\text{stack}} = 6$ , and  $5\text{ s} \times (96 + 1)\text{ times} = 485\text{ s}$  for  $N_{\text{stack}} = 96$ .

The open structure of the RF coil (Fig. 1) inevitably allows environmental RF noise to contaminate the MR signal, yielding a low signal-to-noise ratio. Conductive RF shielding cloth (MS-PY®, Microwave Absorbers Inc., Tokyo, Japan) was

placed beneath the sensor unit (Figs. 5 and ESM5) and connected to the outer shield of the BNC cable (i.e. electric ground) (Fig. 5) to reduce the environmental RF noise as much as possible.

Six plaster samples A, B, C, E, F, and G (see Table ESM2 and Fig. 3) saturated with tap water were prepared. Each water-saturated sample was placed on the sensor unit (e.g. Fig. 5), and transverse proton relaxation data were acquired using the CPMG pulse sequence as described above. The sample and RF coil were wrapped with transparent polyethylene films (10  $\mu\text{m}$  in thickness) during the CPMG measurement to prevent undesirable water evaporation during measurements and to protect the coil from dripping pore water. A 250 mL bottle of a dilute 0.21 wt% aqueous solution of  $\text{CuSO}_4$  [53] was also measured as a standard sample having  $\approx 100$  vol%  $\text{H}_2\text{O}$ . A large value of  $N_{\text{stack}}$  (i.e. 768) was used for this bottle sample because the signal intensity is used to standardize the value of  $\approx 100$  vol%  $\text{H}_2\text{O}$  for the experimental system in Fig. ESM5. Once a reliable signal intensity for this standard sample is obtained with a large value of  $N_{\text{stack}}$ , there is no need to measure the standard sample again if the pulse sequence parameters (e.g. echo spacing) and the magnet are not changed.

Five plaster samples, D, L, M, N, and O (see Table ESM2) saturated with tap water were prepared for the freeze–thawing experiments. First, CPMG data and medical X-ray CT images were acquired before freezing; then the samples were placed in a freezer maintained at  $-14$   $^\circ\text{C}$  for 21 h. As shown in Fig. ESM4e, 93% of the pore water was frozen, which is sufficient to cause frost damage in slaked lime plaster. The frozen samples were left at room temperature to thaw, and then CPMG data were acquired with the same settings as before freezing. Plaster samples were then imaged again by medical X-ray CT to investigate the internal structures altered by the frost damage. The number of the freeze–thaw cycles was unity. The pore size distribution was measured for the plaster sample L in Table ESM2 after the freeze–thaw processing using mercury porosimetry to determine the degree of pore volume expansion induced by pore water freezing.

The principles of CPMG data processing here are based on  $T_2$  relaxometry. The raw time-series data obtained using the CPMG pulse sequence consisted of approximately 1000 echo data points. The first four echoes were truncated and discarded because the initial echoes are transient and distorted due to the grossly inhomogeneous magnetic and RF fields [48]. The transverse relaxation time ( $T_2$ ) for water in porous media often increases with pore diameter [15, 56]. Figures 4 and ESM4a–c show that the pore size distribution is rather broad for all plaster samples prepared, suggesting that the CPMG time-series data are a mixture of exponentially decaying signals with various  $T_2$  values. We employed two models for the CPMG decay curve  $f(t)$  in the present study. One is a simple bi-exponential model that is often

used to analyze CPMG data for heterogeneous multi-phase samples [49, 60, 61]:

$$f(t) = A_{\text{long}} \exp(-t/T_{2\text{long}}) + A_{\text{short}} \exp(-t/T_{2\text{short}}), \quad (1)$$

where  $t$  is time;  $A_{\text{long}}$  and  $A_{\text{short}}$  are the MR signal amplitudes for the long and short  $T_2$  components, respectively; and  $T_{2\text{long}}$  and  $T_{2\text{short}}$  are the  $T_2$  values for the long and short  $T_2$  components, respectively. The four quantities ( $A_{\text{long}}$ ,  $A_{\text{short}}$ ,  $T_{2\text{long}}$ , and  $T_{2\text{short}}$ ) were determined using a conventional least-squares method. We used the simple model given by Eq. (1) to estimate the porosity of the six water-saturated plaster samples.

However, more careful analysis is required to detect the complicated changes in the pore size distribution caused by pore water freezing. Thus, a multi-exponential model [11, 15, 16, 45, 56], which is more advanced, was employed for the evaluation of the frost damage:

$$f(t) = \sum_{i=1}^N A_i \exp(-t/T_{2i}), \quad (2)$$

where  $A_i$  is the MR signal amplitude for the  $i$ th component with a  $T_2$  value of  $T_{2i}$ . The values of  $T_{2i}$  are chosen so that they are equally spaced on a logarithmic scale. In this study,  $N = 200$ , and the maximum and minimum values of  $T_{2i}$  were taken to be 1952 and 0.75 ms, respectively. The software program, UPEN [62], was employed to perform the inverse Laplace transform in Eq. (2) to determine the two hundred unknown quantities,  $A_i$ .

One of the fundamental MR properties,  $T_1$ , was also measured for the water-saturated plaster samples. The conventional saturation recovery measurement [15] with  $N_{\text{stack}} = 70$  was employed. A non-linear fitting method [63] was applied to the recovery curve to obtain  $T_1$  values that were used to correctly set the sequence repetition time,  $TR$ , to satisfy the  $T_1$  full relaxation condition (i.e.  $TR > 5T_1$ ).

$\text{H}_2\text{O}$ – $\text{D}_2\text{O}$  mixtures have been employed to evaluate the accuracy of the proton quantification of MR apparatus [53, 64, 65]. Thus, apart from the slaked lime plaster samples, 250 mL bottles of a  $\text{H}_2\text{O}$ – $\text{D}_2\text{O}$  mixture with a slight amount of  $\text{CuSO}_4$  were measured to examine the proton quantification accuracy for the MR scanner in Fig. ESM5. The  $\text{CuSO}_4$ -doped water samples yield almost the same  $T_2$  values as those for the water-saturated slaked lime plaster samples. The detail of the proton relaxation mechanism for the pore water in porous media is different from that for the  $\text{CuSO}_4$ -doped bulk water [15]. However, a *homogeneous*  $\text{H}_2\text{O}$ – $\text{D}_2\text{O}$  liquid mixture was chosen in the present study because it is an ideal sample compared with the plaster samples, which have a *heterogeneous* structure (see Fig. ESM4a–4c depicting heterogeneous pore distribution) that could reduce the

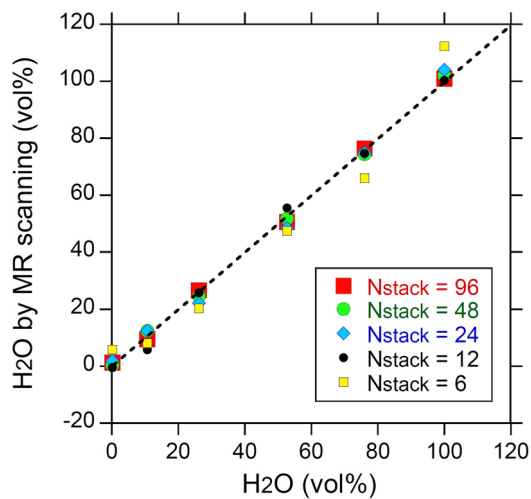


**Fig. 6** Accuracy of water proton quantification by the MR surface scanner obtained by CPMG measurements of  $\text{CuSO}_4$  aqueous solution samples ( $\text{H}_2\text{O}$ – $\text{D}_2\text{O}$  mixture). The calculated RMSE values for  $N_{\text{stack}}$  values of 6, 12, 24, 48, and 96 were 7.7, 2.4, 3.1, 1.5, 1.2 vol%, respectively

estimation accuracy for the proton number in the sensed region. The experimental procedure is described elsewhere [53]. The linear dependence of the CPMG signal intensity on the  $\text{H}_2\text{O}$  volume fraction was examined for  $N_{\text{stack}} = 6, 12, 24, 48, \text{ and } 96$ .

## 3 Results

### 3.1 Measurements of $\text{H}_2\text{O}$ – $\text{D}_2\text{O}$ Mixture

Raw data examples from the CPMG measurements are shown in Fig. ESM6a, and it can be seen that the signal intensity depends on both the  $\text{H}_2\text{O}$  volume fraction and  $N_{\text{stack}}$ . The signal intensity at  $t = 0$  ms,  $A_{\text{long}} + A_{\text{short}}$ , was calculated by fitting Eq. (1) to the CPMG data. The results, shown in Fig. ESM6b, indicate reasonable linearity for the calibration line for all five values of  $N_{\text{stack}}$ .

The accuracy of water proton detection, shown in Fig. 6, was calculated using the calibration lines in Fig. ESM6b. The slight data-point fluctuation can be seen in Fig. 6, and the RMSE value generally degrades as the  $N_{\text{stack}}$  value decreases. The  $\text{H}_2\text{O}$ – $\text{D}_2\text{O}$  mixture samples measured are homogeneous and contain no internal heterogeneity that reduces the accuracy of the calibration lines (see Figs. ESM4abs for the example of the heterogeneous pore structure of plaster samples). Thus, the fluctuation of the data points in Fig. 6 are probably due to the RF noise derived from the electronic devices in the MR scanner and environment. The root mean square error (RMSE) value for  $N_{\text{stack}} = 96$  was as small as 1.2 vol%. It should be noted that this RMSE value is useful as the

basic performance of the MR scanner representing the robustness against the random RF noise only, excluding the effect of the incompleteness of the sample. The RMSE value of 1.2 vol% is smaller than that of 1.6 vol% for  $N_{\text{stack}} = 256$  that was obtained with a single-sided commercial MR scanner (Bruker minispec ProFiler, investigation depth of approximately 3 mm) using the same 250 mL bottles of  $\text{H}_2\text{O}$ – $\text{D}_2\text{O}$  [53], suggesting that our scanner system equipped with the two concentric ring magnets was well designed and constructed.

### 3.2 Measurements of Plaster Porosity

An example of the measurement results for a slaked lime plaster sample is shown in Fig. 7. The sensed region in Fig. 7a determined using the tentative signal cutoffs of 10% and 90% [49, 53] is  $16 \times 12 \text{ mm}^3$ . However, Fig. 2 and ESM3 suggest that the sensed region seep out of the yellow dotted rectangle in Fig. 7a. Thus, it should be noted that pore water located out of the yellow dotted rectangle also contributes to the MR signals acquired.

Two  $T_1$  values (i.e. 46 and 914 ms) were obtained using the bi-exponential model for the recovery of the nuclear magnetization (Fig. 7b). It should be noted that even the longest component (914 ms) satisfies the  $T_1$  full relaxation condition that the sequence repetition time (5 s) should be larger than five times the  $T_1$  value, which is essential for reliable porosity measurements using the CPMG method.

The CPMG data obtained under the  $T_1$  full-relaxation condition were converted into porosity values (i.e. the water volume fraction value of the saturated porous sample) as follows. An example of the CPMG data is shown in Fig. 7c and ESM8, depicting the evident proton signal from the water-saturated plaster sample B. Equation (1) was well fitted to the CPMG data to obtain the sum of  $A_{\text{long}} + A_{\text{short}}$ , which is proportional to the amount of water molecules in the sensed region. For example, the quantity  $A_{\text{long}} + A_{\text{short}}$  was 554,000 for the 250 mL  $\text{H}_2\text{O}$  bottle sample ( $N_{\text{stack}} = 768$ ), and 28,700 for the water-saturated plaster sample in Fig. 3 ( $N_{\text{stack}} = 96$ ), with the data shown respectively in Figs. ESM8 and 7c. Thus, the porosity of the plaster sample B was calculated to be  $28,700 \times 768 / (554,000 \times 96) = 41.4 \text{ vol\%}$ , which agrees well with the ground truth porosity value (43.6 vol%, see Table ESM2) determined by the weight difference between the dried and saturated states.

The results of the porosity measurements of the six water-saturated plaster samples by MR scanning are summarized in Fig. 8. Each sample was scanned twice, and thus the total number of the data points is twelve for each  $N_{\text{stack}}$  value. The RMSE value for the twelve data points was 9.3, 7.2, 7.4, 3.3, and 1.9 vol%, for  $N_{\text{stack}} = 6, 12, 24, 48, \text{ and } 96$ , respectively. Due to contamination by RF noise derived from the electronic devices in the MR scanner and environment, these



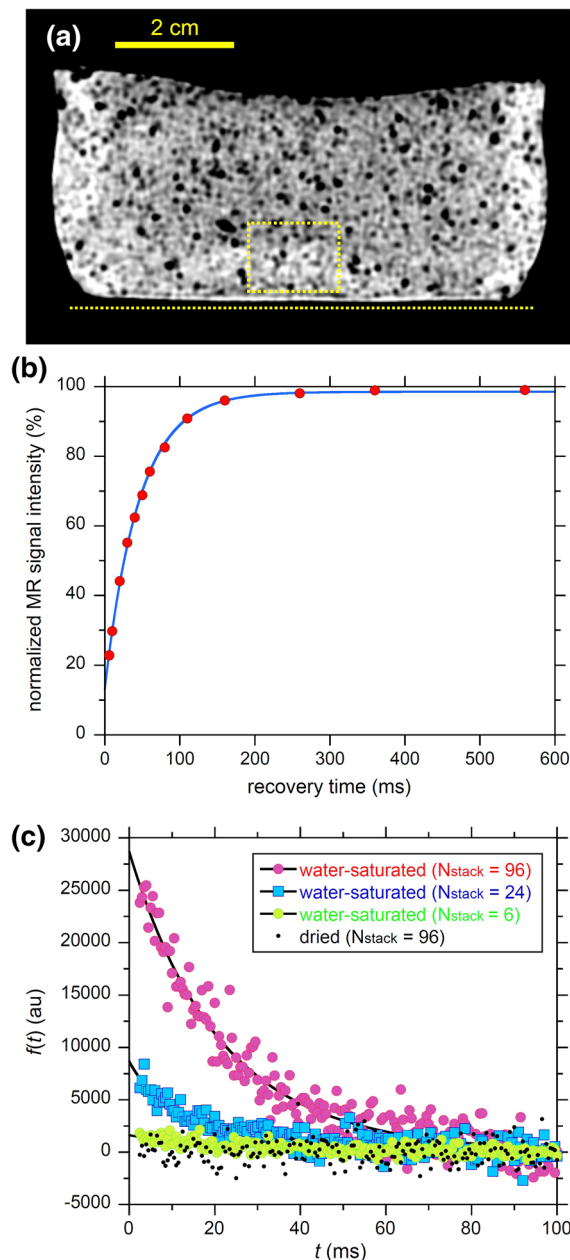


**Fig. 7** Results for the slaked lime plaster sample B shown in Fig. 3. **a** Two-dimensional X-ray CT image of the water-saturated sample obtained by a medical CT scanner. The approximate locations of the sensed region ( $16 \times 12$  mm) and the copper wire for the planar RF coil when being measured in Fig. 5 are marked by a yellow dotted rectangle and a line, respectively. **b**  $T_1$  relaxation process for the water-saturated sample obtained by the saturation recovery method. A full-range plot is shown in Fig. ESM7. A bi-exponential model (solid line) was fitted to the recovery curve to obtain two  $T_1$  values, namely, 46 ms as a major component, and 914 ms as a trace component. **c**  $T_2$  relaxation process acquired by CPMG experiments for the water-saturated state for three  $N_{\text{stack}}$  values and for the dried state (Fig. ESM4a) for a single  $N_{\text{stack}}$  value. A full-range plot is shown in Fig. ESM8. A bi-exponential model, given by Eq. (1), was fitted to the CPMG data for the water-saturated state using the least-squares method (solid line). The fitted values ( $A_{\text{long}}$ ,  $A_{\text{short}}$ ,  $T_{2\text{long}}$ , and  $T_{2\text{short}}$ ) for the three water-saturated samples were (19096, 9595, 25.1 ms, 15.9 ms), (5372, 3299, 26.4 ms, 5.8 ms), and (1134, 480, 27.3 ms, 22.9 ms) for  $N_{\text{stack}} = 96, 24,$  and 6, respectively

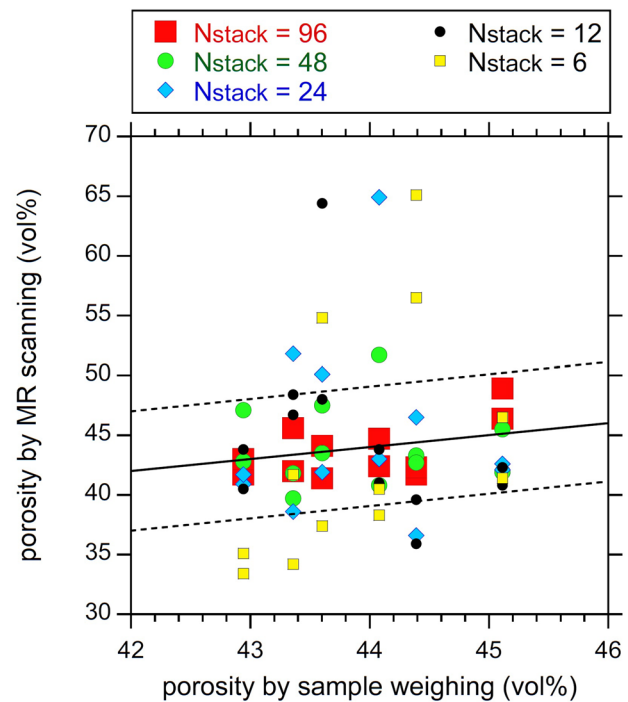


**Fig. 8** Accuracy of MR scanning for six water-saturated intact plaster samples (samples A, B, C, E, F, and G listed in Table ESM2) for various  $N_{\text{stack}}$  values. The horizontal axis is the porosity conventionally obtained by weighing the difference between dried and water-saturated plaster samples. Three error contours, corresponding to 0 and  $\pm 5$  vol%, are indicated by solid and dotted lines, respectively. The RMSE value was 9.3, 7.2, 7.4, 3.3, and 1.9 vol% for  $N_{\text{stack}} = 6, 12, 24, 48$  and 96, respectively

RMSE values increase with decreasing  $N_{\text{stack}}$ , which was also observed for the  $\text{H}_2\text{O}-\text{D}_2\text{O}$  mixture samples (Fig. 6). Due to the signal stacking, the twelve data points for  $N_{\text{stack}} = 96$  converge reasonably and are located very near the ground truth line with 0% error in Fig. 8. This convergence on the ground truth line suggests that the MR data acquired were not biased and the experiments were performed in a reliable manner. The RMSE value for the plaster sample is slightly worse than that for the  $\text{H}_2\text{O}-\text{D}_2\text{O}$  sample for each  $N_{\text{stack}}$ . This is probably due to the difference in the  $\text{H}_2\text{O}$  amount in the sensed region (i.e.  $\approx 44$  vol% for the plaster vs.  $\approx 100$  vol% for the  $\text{H}_2\text{O}-\text{D}_2\text{O}$  mixture at the maximum) and to the heterogeneity of the spatial pore distribution in the plaster (Figs. 7a and ESM4a, b, c) as compared with the homogeneity of the  $\text{H}_2\text{O}-\text{D}_2\text{O}$  mixture.

### 3.3 Freeze–Thawing Experiments

The results of the freeze–thaw experiments were almost the same for all five plaster samples measured. The results for one plaster sample are shown in Fig. 9, and those for a different sample are shown in Fig. ESM9. The results for the remaining three samples were reported elsewhere [51].



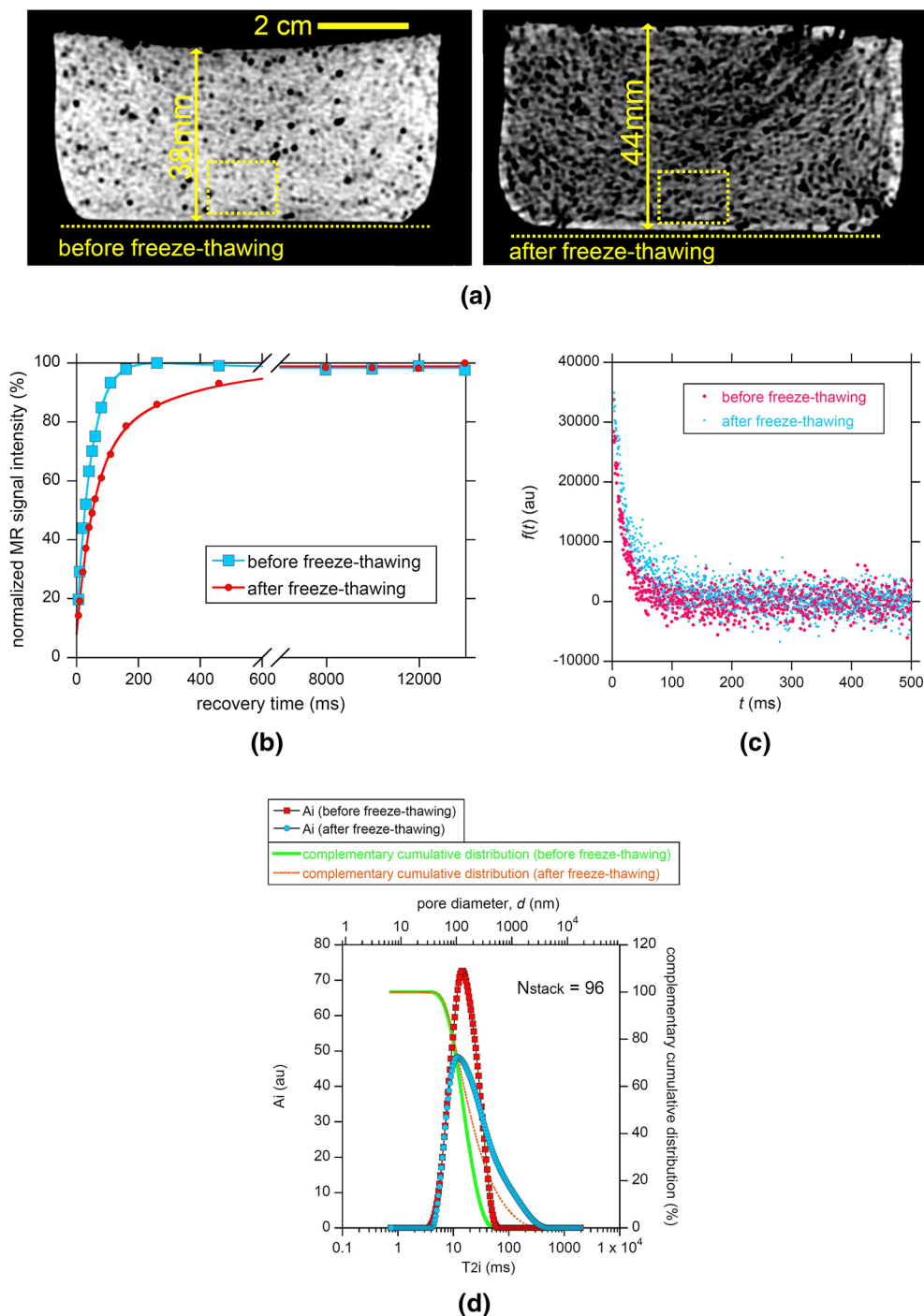


**Fig. 9** Results of freeze–thaw experiments for a water-saturated slaked lime plaster sample (sample L listed in Table ESM2). **a** Two-dimensional X-ray CT images. The grey scales for the two images are common. Almost the same location was scanned before and after the freeze–thaw processing. The approximate locations of the sensed region ( $16 \times 12$  mm) and the copper wire for the planar RF coil when being measured by the MR surface scanner are marked by a yellow dotted rectangle and a line, respectively. While the length indicated by the yellow arrow is 38 mm before freeze–thawing, it increases to 44 mm after freeze–thawing due to the freezing-driven pore volume expansion. **b**  $T_1$  relaxation dependence on the freeze–thaw processing. Note that the  $T_1$  relaxation after freeze–thawing is slower than that before freeze–thawing. A bi-exponential model (solid line) was fitted to the recovery curve

to obtain two  $T_1$  values, namely, 47 ms as a major component and 267 ms as a minor component before freeze–thawing, and 55 ms as a major component and 306 ms as a minor component after freeze–thawing. **c**  $T_2$  relaxation process acquired from the CPMG experiments for the water-saturated state with  $N_{\text{stack}} = 96$ . Note the delayed  $T_2$  relaxation after freeze–thawing compared with that before freeze–thawing. **d**  $T_2$  distribution for the time-series data in **c**. The areas of the two distributions are the same. The complementary cumulative distribution integrated from the maximum value of  $T_{2i}$  is also plotted. The  $T_2$  values on the horizontal axis are converted into the cylindrical pore diameter,  $d$ , using  $d = 4r_2T_2$  where  $\rho_2 = 2.2 \mu\text{m/s}$

Example medical X-ray CT images of the plaster samples are shown in Fig. 9a, demonstrating the effects of the freeze-thaw processing. Bright and dark pixels in the CT images correspond to local high- and low-density areas, respectively. The plaster CT image after freeze-thawing is almost entirely dark compared with the image before freeze-thawing, suggesting that the plaster sample expanded due to freezing of the pore water. The difference in the sample height before and after freeze-thawing (i.e. 38 mm vs. 44 mm) also supports this interpretation.

The  $T_1$  recovery curves for the plaster sample in Fig. 9a are shown in Fig. 9b, and these also demonstrate the effects of freeze-thawing. The  $T_1$  value for the pore water in porous media increases with increasing pore size [11, 15]. Figure 9b clearly shows that the  $T_1$  value after freeze-thawing is significantly longer than that before freeze-thawing. This also suggests that the pore size increased during the freeze-thaw processing, consistent with the observations shown in Fig. 9a.

The CPMG data shown in Fig. 9c demonstrate that the  $T_2$  relaxation of the sample after freeze-thawing occurs more slowly than that before freeze-thawing. This difference in the  $T_2$  value observed in the time domain is depicted more evidently in the  $T_2$  spectrum domain in Fig. 9d obtained by fitting Eq. (2) using the UPEN program. Multi-component  $T_2$  analysis (Eq. 2) with  $N = 200$  reveals the fine structure of the  $T_2$  distribution. As will be discussed in the next section, the  $T_2$  value for porous media increases with increasing pore size, and thus the  $T_2$  distribution can be converted into the pore size distribution [11, 15]. The  $T_2$  distribution and the corresponding complementary cumulative distribution shift in the direction of increasing  $T_2$  after freeze-thawing in Fig. 9d. This implies that the pore size increases during freeze-thawing due to pore water freezing, which is consistent with the results seen in Fig. 9a, b.

Mercury porosimetry was applied to the sample shown in Fig. 9 after freeze-thawing to reveal the effects of freezing on the pore size distribution for the samples kneaded at 41.2 wt% H<sub>2</sub>O. The results are shown in Fig. 4, and it can be seen that a significant fraction of pores with a diameter of approximately 1000–2000 nm become larger (approximately 2000 to 10,000 nm). This is consistent with the experimental results shown in Fig. 9, suggesting that pore expansion indeed occurs due to the pore water freezing.

The results for another plaster sample are shown in Fig. ESM9. All four panels (a–d) demonstrate again that the pore size increased due to the freeze-thaw processing, consistent with the results shown in Fig. 9. The effect of the  $N_{\text{stack}}$  value is shown in Fig. ESM10. The  $T_2$  distribution and the complementary cumulative distribution in Figs. ESM10a and ESM10b ( $N_{\text{stack}} = 6$ ) are slightly different from those in Figs. 9d and ESM9d ( $N_{\text{stack}} = 96$ ), respectively, probably due to the random noise contaminating the CPMG time-domain data (see Fig. 7c). However, Figs. ESM10a and 10b show

that the  $T_2$  spectrum and the complementary cumulative distribution after freeze-thawing shift in the direction of the  $T_2$  increase, suggesting again that the pore size increased during freeze-thawing, which is consistent with the results in Fig. 9d and ESM9d.

## 4 Discussion

### 4.1 MR Properties of Porous Plaster

The  $T_1$  and  $T_2$  surface relaxivities ( $\rho_1$  and  $\rho_2$ , respectively) are important fundamental properties of porous media because  $\rho_1$  and  $\rho_2$  allow for the calculation of the  $T_1$  and  $T_2$  values, respectively, if the surface-to-volume ratio for the porous media,  $(S/V)_{\text{pore}}$ , is known [11, 15]. The relaxation data for  $T_1$  and  $T_2$  obtained in the present study enable us to calculate  $\rho_1$  and  $\rho_2$  for the water-saturated slaked lime plaster samples as follows. By applying a mono-exponential model (i.e.  $N = 1$  for Eq. 2) to Figs. 7b, 9b, and ESM9b, three  $T_1$  values were determined to be 46, 44, and 42 ms (average, 44 ms) for the intact plaster samples; three  $T_2$  values were also determined based on Figs. 7c, 9c, and ESM9c to be 22, 18, and 19 ms (average, 20 ms) for  $N_{\text{stack}} = 96$ . According to Fig. 4, the  $(S/V)_{\text{pore}}$  is  $2.3 \times 10^7$  1/m for the intact sample kneaded with 41.2 wt% H<sub>2</sub>O. Thus, according to the conventional method [11, 15],  $\rho_1$  was calculated to be  $1/(44 \text{ ms} \times 2.3 \times 10^7 \text{ 1/m}) = 0.99 \text{ } \mu\text{m/s}$ , and  $\rho_2$  was calculated to be  $1/(20 \text{ ms} \times 2.3 \times 10^7 \text{ 1/m}) = 2.2 \text{ } \mu\text{m/s}$  for the intact water-saturated porous plaster samples.

These  $\rho_1$  and  $\rho_2$  values are relatively small compared with those for natural sedimentary rocks with paramagnetic iron-bearing minerals [15] accelerating proton relaxation of the pore water molecules near the mineral surfaces. According to Fig. ESM4d, the main components in slaked lime plaster are portlandite and calcite, which are both diamagnetic minerals [39]. Generally,  $\rho_1$  and  $\rho_2$  for diamagnetic minerals are small due to the absence of unpaired electrons [66–68]. Thus, these small  $\rho_1$  and  $\rho_2$  values for the slaked lime plaster samples are a consequence of this diamagnetic property of portlandite and calcite.

The small  $\rho_2$  value enables us to convert the  $T_2$  distribution into a pore size distribution as follows [11, 15]. Applying a cylindrical pore model to Fig. 4, the characteristic pore diameter for the plaster sample is calculated to be  $4/(S/V)_{\text{pore}} = 170 \text{ nm}$ . Thus, the product of the pore diameter and  $\rho_2$ , a measure of the  $T_2$  relaxation effect on the solid-water interface, is  $170 \text{ nm} \times 2.2 \text{ } \mu\text{m/s} = 3.7 \times 10^{-13} \text{ m}^2/\text{s}$ . Because it is much smaller than the self-diffusivity of water molecules at room temperature ( $\approx 2 \times 10^{-9} \text{ m}^2/\text{s}$ ), the  $T_2$  relaxation for pore water is under the *fast-diffusion regime*, which allows for the conversion of the  $T_2$  value into pore diameter,  $d$ , as

$d = 4\rho_2T_2$  [11, 15]. This conversion is implemented in the horizontal axes of Figs. 9d, ESM9d, and ESM10ab.

## 4.2 Porosity Measurements

The experimental results in Fig. 8 show that accurate moisture quantification was performed successfully for the intact water-saturated slaked lime plaster samples using the constructed sensor unit. The RMSE value was 1.9 vol% for  $N_{\text{stack}} = 96$ , which is almost the same as that reported for porous sedimentary rocks using different single-sided MR scanners [15, 42, 69]. Thus, the performance of the sensor unit (Fig. 1) with a carefully designed magnetic circuit (Fig. ESM2) is reasonable, and the single-sided MR scanner system (Fig. ESM5) is a promising non-destructive tool for in situ moisture quantification of heritage architecture made of slaked lime plaster (e.g. walls and roofs).

Because  $\rho_2$  values depend on the chemistry and mineralogy of the porous media [15, 66–68],  $T_2$  values of the CPMG data also depend on those of building materials. However, it should be noted that the calibration line (i.e. solid line as the ground truth) in Fig. 8 was drawn using only the signal intensity for the reference sample of bulk water as 100 vol%  $\text{H}_2\text{O}$ . Thus, the calibration line in Fig. 8 would be also applicable to the porosity measurements of building materials other than slaked lime plaster (e.g. stones and bricks) [16, 19, 42, 43, 45–47].

The scanner system with the mobile sensor unit is portable and works with an AC 100-V power supply. The next step would be to operate the scanner in open-air conditions. Outdoor experiments are currently in progress [51], and the preliminary results have shown promise. For example, the same plaster sample as that in Fig. 3 was measured successfully outdoors, as shown in Fig. ESM11. Thus, the results demonstrate that the portable MR surface scanner could be used as a non-destructive testing tool for the in situ moisture measurement of heritage architecture in open-air conditions.

One potential use of the MR surface scanner in the open air is to monitor the drying of building materials [8], for example, the drying of fresh wet plaster in construction management for the remediation of architectural features such as castle walls. The  $\text{Ca}(\text{OH})_2$  grains in the plaster react with the atmospheric  $\text{CO}_2$  to form  $\text{CaCO}_3$  grains, which causes mechanical hardening of the plaster [28–30, 33]. The moisture in the porous plaster is critical because water-filled pores inhibit the reaction of  $\text{Ca}(\text{OH})_2$  and  $\text{CO}_2$ , resulting in delayed hardening. Preliminary laboratory experiments to monitor a drying plaster plate sample was performed using the system in Fig. ESM5 [51]. As the drying process proceeds, the four quantities ( $A_{\text{long}}$ ,  $A_{\text{short}}$ ,  $T_{2\text{long}}$ , and  $T_{2\text{short}}$ ) in Eq. (1) decreased, yielding CPMG signals with worse signal-to-noise ratios. However, the results indicated a good linear relationship between the decreasing MR signal intensity (i.e.

$A_{\text{long}} + A_{\text{short}}$ ) and the decreasing plate weight. These preliminary results suggest that the MR surface scanner is suitable for monitoring the drying of fresh wet plaster in construction management of heritage architecture.

The following three items, (i) to (iii), should be noted as the further research steps for the practical use of the MR scanner for the maintenance and remediation of the heritage architecture.

**(i) Downsizing** The console system (Fig. ESM5) was originally developed for the measurements of live cattle at cowsheds with an investigation depth of 3 cm [49]. Thus, it is overengineered for the shallower investigation depth of approximately 1 cm (Fig. 2). The console is large and as heavy as  $\approx 120$  kg, making it difficult to use on small scaffolds at construction sites of the heritage architecture. It would be technically possible to downsize the console by replacing with a small laptop computer and a lightweight NMR amplifier [60].

**(ii) Relaxivity measurement** Even if the building material of the heritage architecture is not slaked lime plaster, the water volume fraction could be accurately quantified using the single-sided MR scanner without the information of the  $\rho_2$  value that depends on the chemistry and mineralogy of the building material [16, 19, 42, 43, 45–47]. However, the measurement of the  $\rho_2$  value is essential to convert the  $T_2$  distribution into the pore size distribution using  $d = 4\rho_2T_2$  (Figs. 9 and ESM9 and 10). The surface relaxivity value determined in the present study (i.e.  $\rho_2 = 2.2 \mu\text{m/s}$ ) is valid only for the plaster powder product. The  $\rho_2$  value depends on the chemical and mineral compositions (e.g. contents of iron-bearing paramagnetic minerals) of the porous media [15, 66–68]. Thus, when applying the MR scanner to the pore size distribution measurement of building materials other than slaked lime plaster, laboratory measurements of the  $\rho_2$  value for the building materials are needed for the accurate conversion of the  $T_2$  distribution into the pore size distribution.

**(iii) Reduction of the measurement time** The reduction of the measurement time, approximately calculated as  $TR \times N_{\text{stack}}$ , required for CPMG data acquisition for a single area is a key to enabling rapid moisture mapping of the large walls and roofs of heritage architecture. The following three items, (a) to (c), should be noted with respect to the measurement time reduction: (a) The environmental RF noise shield with the metallic Faraday cage is effective for the improvement of the signal-to-noise ratio of the raw CPMG data [70], resulting in the reduction of the number of stacked signals,  $N_{\text{stack}}$ . The current RF shield using the conductive shield cloth (Fig. 5) is insufficient because only a single face (i.e. bottom face) of the magnetic circuit is covered. The full-face shielding of the sensor unit using conductive copper films is being performed (unpublished data). The preliminary

results show that the random noise level in the CPMG data is successfully reduced to approximately 50%, which would contribute to the reduction of  $N_{\text{stack}}$  to approximately 25%. (b) A trace component as long as  $T_1 = 914$  ms is observed in Fig. 7b using a bi-exponential analysis, which leads to  $TR = 5$  s in order to meet the full relaxation condition in the present study. According to the recovery curve in Fig. 7b, however, the contribution of the trace component is small, and the nuclear magnetization almost completely recovers within several hundred milliseconds (see also Fig. ESM7). Almost all of the nuclear magnetization recovers within a second even for samples after the freeze-thaw processing (Figs. 9b and ESM9b). Thus, measurements with  $TR \approx 1$  s could be acceptable for practical use, which would reduce the measurement time greatly. (c) The  $N_{\text{stack}}$  value required for the accurate porosity measurement depends on the intensity of the environmental RF noise. For example,  $N_{\text{stack}} = 96$  was required to obtain  $\text{RMSE} = 1.9$  vol% (Fig. 8) in the noisy laboratory (Fig. ESM5) where many electronic devices were working. Fortunately, in contrast, according to the results from the preliminary experiment in open-air conditions, the noise level was significantly smaller than in the laboratory (Fig. ESM11c). Thus, if the heritage architecture is located in a quiet place or the countryside, as was the case for the measurements shown in Fig. ESM11, the RF noise is minimal, and we could choose a smaller value for  $N_{\text{stack}}$ , resulting in a reduction of the measurement time.

### 4.3 Detection of Frost Damage

All data for mercury porosimetry (Fig. 4), X-ray CT (Figs. 9a, ESM9a),  $T_1$  recovery (Figs. 9b, ESM9b), and  $T_2$  relaxation (Figs. 9c, d, ESM9cd, and ESM10ab) show that pore expansion occurred in the slaked lime plaster samples due to the frost damage simulated in the laboratory. Particularly, Figs. 9d, ESM9d, and ESM10ab revealed that the  $T_2$  distribution after freeze–thawing is rather different from that before freeze–thawing. The present study demonstrated for the first time that the noisy CPMG data acquired using a single-sided MR scanner is useful for detecting the change in pore size caused by pore water freezing for slaked lime plaster. Thus, the use of the MR scanner developed is promising for the in situ detection of frost damage, such as in heritage architecture in cold regions.

The following two items should be noted. (i) Generally, the signal-to-noise ratio for the single-sided MR scanner is worse compared with that for the bi-lateral MR apparatus [53]. As a result, a long measurement time (i.e. 485 s) with  $N_{\text{stack}} = 96$  was required to ensure the RMSE value of 1.9 vol% (Fig. 8). However, Fig. ESM10 shows that  $N_{\text{stack}} = 6$  (i.e. 35 s) is sufficient for the qualitative detection of the frost damage. This would contribute to the reduction of the measurement time for the practical use in the construction management. (ii)

It should be noted that a single freeze-thaw cycle yielded a detectable serious damage in the plaster samples (Figs. 9 and ESM9). In contrast, no serious frost damage was detected after a few cycles for concrete samples much harder than plaster samples [71]. Thus, careful monitoring of the frost damage is required for the remediation project of heritage architecture using fresh wet slaked lime plaster [54] in cold regions.

The plaster samples showed homogeneous pore volume expansion, as depicted in Figs. 9a and ESM9a, in the present study. Another type of sample expansion, heterogeneous volume expansion, (i.e. cracking) could be induced by frost damage [38]. The single-sided MR scanner can also detect the formation of such cracks if the cracks are located in the sensed region of the sensor unit. This is because the  $T_2$  value for water protons in a crack with an aperture larger than a few millimeters is significantly larger than that in the microscopic pores in intact plaster. Although the fast-diffusion regime [11, 15] breaks down for these cracks, careful analysis of the  $T_2$  distribution [72] would allow for the estimation of the aperture size for water-filled cracks hidden beneath the surface of plaster walls and roofs.

In the present study, a single-sided MR surface scanner was successfully used to detect frost damage (Figs. 9, ESM9, and ESM10) in slaked lime plaster samples. MR scanning using the CPMG pulse sequence followed by multi-exponential analysis could also be performed for building materials different from slaked lime plaster [14, 16, 17, 19, 20, 40–45], namely, natural stone, cement, and gypsum plaster. Thus, the single-sided MR scanner may also be a promising tool for the non-destructive in situ detection of frost damage in heritage architecture made of various kinds of building materials in cold regions.

## 5 Conclusions

A mobile MR sensor unit employing two concentric ring magnets was designed and constructed for the non-destructive in situ quantification of the moisture in plaster walls and roofs of heritage architecture. Laboratory experiments on water-saturated porous slaked lime plaster samples were performed. The porosity (water volume fraction) and the fundamental MR-related property, surface relaxivity, were measured successfully for the samples. The effects of frost damage on the sample volume expansion induced by pore water freezing was also measured successfully using  $T_2$  relaxometry. These results demonstrate that the MR surface scanner is a promising non-destructive tool for the maintenance and remediation of heritage architecture made of slaked lime plaster (e.g. monitoring of drying of fresh wet plaster in construction management and detection of frost damage).



**Supplementary Information** The online version contains supplementary material available at <https://doi.org/10.1007/s10921-023-00998-y>.

**Acknowledgements** Comments by three reviewers were helpful. The medical X-ray CT scans of the plaster samples were performed at GSJ-Lab, AIST. X-ray microtomographic imaging of the plaster samples was conducted with support from the NIMS microstructural characterization platform, a program of the “Nanotechnology Platform” of the Ministry of Education, Culture, Sports, Science and Technology (MEXT), Japan (Grant No. JPMXP09A21NM0106). A bi-lateral MR apparatus was used for low-temperature proton relaxation measurements of the plaster samples at the Center for Instrumental Analysis, Gunma University (Kiryu, Gunma).

**Funding** The authors have not disclosed any funding.

**Data Availability** Some parts of the datasets generated during the study are available from the author on reasonable request.

## Declarations

**Conflict of interest** The authors declare no competing interests.

**Ethical Approval** All ethical COPE guidelines have been considered.

**Consent for Publication** Not applicable.

**Open Access** This article is licensed under a Creative Commons Attribution 4.0 International License, which permits use, sharing, adaptation, distribution and reproduction in any medium or format, as long as you give appropriate credit to the original author(s) and the source, provide a link to the Creative Commons licence, and indicate if changes were made. The images or other third party material in this article are included in the article’s Creative Commons licence, unless indicated otherwise in a credit line to the material. If material is not included in the article’s Creative Commons licence and your intended use is not permitted by statutory regulation or exceeds the permitted use, you will need to obtain permission directly from the copyright holder. To view a copy of this licence, visit <http://creativecommons.org/licenses/by/4.0/>.

## References

- Blümich, B., Perlo, J., Casanova, F.: Mobile single-sided NMR. *Prog. Nucl. Magn. Reson. Spectrosc.* **52**, 197–269 (2008)
- Casanova, F., Perlo, J., Blümich, B. (eds.): *Single-Sided NMR*. Springer, Heidelberg (2011)
- Blümich, B., Anders, J.: When the MOUSE leaves the house. *Magn. Reson.* **2**, 149–160 (2021)
- Marble, A.E., Mastikhin, I.V., Colpitts, B.G., et al.: An analytical methodology for magnetic field control in unilateral NMR. *J. Magn. Reson.* **174**, 78–87 (2005)
- Fukushima, E., Jackson, J.A.: Unilateral magnet having a remote uniform field region for nuclear magnetic resonance. US Patent 6,828,892 (2004)
- de Oliveira-Silva, R., Lucas-Oliveira, É., de Araújo-Ferreira, A.G., et al.: A benchtop single-sided magnet with NMR well-logging tool specifications-examples of application. *J. Magn. Reson.* **322**, 106871 (2021)
- Wolter, B., Dobmann, G., Herzer, H., Bloem, P.: One-sided access NMR for concrete inspection. *Proc. Eur. Conf. Nondestruct. Test.* **1**, 975–982 (1998)
- Wolter, B., Dobmann, G., Sourkova, N., et al.: Kernresonanz in aufsatztechnik (Nuclear magnetic resonance in one-sided access technique). *Tech. Mess.* **69**, 43–48 (2002)
- Guthausen, A., Zimmer, G., Blumler, P., Blümich, B.: Analysis of polymer materials by surface NMR via the MOUSE. *J. Magn. Reson.* **130**, 1–7 (1998)
- Kleinberg, R.L., Sezginer, A., Griffin, D.D., Fukuhara, M.: Novel NMR apparatus for investigating an external sample. *J. Magn. Reson.* **97**, 466–485 (1992)
- Coates, G.R., Xiao, L., Prammer, M.G.: *NMR Logging Principles and Applications*. Gulf Professional Publishing, Houston (2001)
- Li, J., Mailhot, S., Kantola, A.M., et al.: Longitudinal single-sided NMR study: silica-to-alumina ratio changes the reaction mechanism of geopolymer. *Cem. Concr. Res.* **160**, 106921 (2022)
- Costabel, S., Hiller, T., Dlugosch, R., et al.: Evaluation of single-sided nuclear magnetic resonance technology for usage in geosciences. *Meas. Sci. Technol.* **34**, 015112 (2023)
- Nagel, S.M., Strangfeld, C., Kruschwitz, S.J.: Application of  $^1\text{H}$  proton NMR relaxometry to building materials—a review. *J. Magn. Reson. Open.* **6–7**, 100012 (2021)
- Dunn, K.-J., Bergman, D.J., LaTorraca, G.A.: *Nuclear Magnetic Resonance: Petrophysical and Logging Applications*. Pergamon, Amsterdam (2002)
- Capitani, D., Di Tullio, V., Proietti, N.: Nuclear magnetic resonance to characterize and monitor cultural heritage. *Prog. Nucl. Magn. Reson. Spectrosc.* **64**, 29–69 (2012)
- Braun, F., Orłowski, J.: Non-destructive detection of the efficiency of long-term weathered hydrophobic natural stones using single-sided NMR. *J. Cult. Herit.* **41**, 51–60 (2020)
- Fukunaga, K., Meldrum, T., Zia, W., et al.: Nondestructive investigation of the internal structure of fresco paintings. In: *IEEE 2013 Digital Heritage International Congress*. vol. 1, pp. 81–88 (2013)
- Haber, A., Blümich, B., Souvorova, D., et al.: Ancient Roman wall paintings mapped nondestructively by portable NMR. *Anal. Bioanal. Chem.* **401**, 1441–1452 (2011)
- Blümich, B., Haber, A., Casanova, F., et al.: Noninvasive depth profiling of walls by portable nuclear magnetic resonance. *Anal. Bioanal. Chem.* **397**, 3117–3125 (2010)
- Phillipson, M.C., Baker, P.H., Davies, M., Ye, Z., McNaughtan, A., Galbraith, G.H., McLean, R.C.: Moisture measurement in building materials: an overview of current methods and new approaches. *Build. Serv. Eng. Res. Technol.* **28**, 303–316 (2007)
- Watanabe, A., Furukawa, H., Miyamoto, S., Minagawa, H.: Non-destructive chemical analysis of water and chlorine content in cement paste using near-infrared spectroscopy. *Constr. Build. Mater.* **196**, 95–104 (2019)
- Martínez-Garrido, M.I., Fort, R., Gómez-Heras, M., Valles-Iriso, J., Varas-Muriel, M.J.: A comprehensive study for moisture control in cultural heritage using non-destructive techniques. *J. Appl. Geophys.* **155**, 36–52 (2018)
- El Masri, Y., Rakha, T.: A scoping review of non-destructive testing (NDT) techniques in building performance diagnostic inspections. *Constr. Build. Mater.* **265**, 120542 (2020)
- Camuffo, D.: Standardization activity in the evaluation of moisture content. *J. Cult. Herit.* **31**, S10–S14 (2018)
- Martinho, E., Dionísio, A.: Main geophysical techniques used for non-destructive evaluation in cultural built heritage: a review. *J. Geophys. Eng.* **11**, 053001 (2014)
- Tanabe, T., Kanai, T., Kuroo, K., Nishiwaki, T., Oyama, Y.: Non-contact terahertz inspection of water content in concrete of infrastructure buildings. *World J. Eng. Technol.* **6**, 275–281 (2018)
- Hashimoto, S., Shimoda, W., Takeda, H., et al.: Fabrication of slaked lime compacts (plasters) with high compressive strength using a warm press method. *Build. Mater.* **110**, 65–69 (2016)

29. Cizer, Ö., Rodrigues-Navarro, C., Ruiz-Agudo, E., et al.: Phase and morphology evolution of calcium carbonate precipitated by carbonation of hydrated lime. *J. Mater. Sci.* **47**, 6151–6165 (2012)
30. Yamaguchi, K., Hashimoto, S., Nagata, Y., et al.: Rapid fabrication of frescoes using a geomimetic ceramic formation process. *Ceram. Int.* **48**, 4858–4866 (2022)
31. Subramaniam, S.R.: A review on repair and rehabilitation of heritage buildings. *Int. Res. J. Eng. Technol.* **3**, 1330–1336 (2016)
32. Oka, K., Tamura, M., Maruyama, H., et al.: Experimental study on conservation and preservation for historical architecture using plaster finishing material. In: *Proceedings Fourth International Conference on Sustainable Construction Materials and Technologies* (2016)
33. Elert, K., Rodriguez-Navarro, C., Pardo, E.S., et al.: Lime mortars for the conservation of historic buildings. *Stud. Conserv.* **47**, 62–75 (2002)
34. Veiga, R.: Air lime mortars: what else do we need to know to apply them in conservation and rehabilitation interventions? A review. *Constr. Build. Mater.* **157**, 132–140 (2017)
35. Urankar, M., Bokan-Bosiljkov, V.: Influence of freeze–thaw cycles on mechanical properties of historical brick masonry. *Constr. Build. Mater.* **84**, 416–428 (2015)
36. Di Bella, G., Fiore, V., Galtieri, G., et al.: Effects of natural fibres reinforcement in lime plasters (kenaf and sisal vs. polypropylene). *Constr. Build. Mater.* **58**, 159–165 (2014)
37. Vejmelková, E., Keppert, M., Keršner, Z., et al.: Mechanical, fracture-mechanical, hydric, thermal, and durability properties of lime–metakaolin plasters for renovation of historical buildings. *Constr. Build. Mater.* **31**, 22–28 (2012)
38. Török, Á., Szemerey-Kiss, B.: Freeze-thaw durability of repair mortars and porous limestone: compatibility issues. *Prog. Earth Planet. Sci.* **6**, 1–12 (2019)
39. Haynes, W.M. (ed.): *CRC Handbook of Chemistry and Physics*, 91st edn. CRC Press, Boca Raton (2011)
40. Oligschläger, D., Waldow, S., Haber, A., et al.: Moisture dynamics in wall paintings monitored by single-sided NMR. *Magn. Reson. Chem.* **53**, 48–57 (2015)
41. Capitani, D., Proietti, N., Gobino, M., et al.: An integrated study for mapping the moisture distribution in an ancient damaged wall painting. *Anal. Bioanal. Chem.* **395**, 2245–2253 (2009)
42. Keine, S., Holthausen, R.S., Raupach, M.: Single-sided NMR as a non-destructive method for quality evaluation of hydrophobic treatments on natural stones. *J. Cult. Herit.* **36**, 128–134 (2019)
43. Poli, T., Toniolo, L., Valentini, M., et al.: A portable NMR device for the evaluation of water presence in building materials. *J. Cult. Herit.* **8**, 134–140 (2007)
44. Rehorn, C., Blümich, B.: Cultural heritage studies with mobile NMR. *Angew. Chem. Int. Ed.* **57**, 7304–7312 (2018)
45. Sharma, S., Casanova, F., Wache, W., et al.: Analysis of historical porous building materials by the NMR-MOUSE. *Magn. Reson. Imaging.* **21**, 249–255 (2003)
46. Stagno, V., Genova, C., Zoratto, N., Favero, G., et al.: Single-sided portable NMR investigation to assess and monitor cleaning action of PVA-borax hydrogel in travertine and Lecce stone. *Molecules.* **26**, 3697 (2021)
47. Stagno, V., Ciccola, A., Curini, R., et al.: Non-invasive assessment of PVA-borax hydrogel effectiveness in removing metal corrosion products on stones by portable NMR. *Gels.* **7**, 265 (2021)
48. Hürlimann, M.D., Griffin, D.D.: Spin dynamics of Carr–Purcell–Meiboom–Gill-like sequences in grossly inhomogeneous  $B_0$  and  $B_1$  fields and application to NMR well logging. *J. Magn. Reson.* **143**, 120–135 (2000)
49. Nakashima, Y.: Development of a single-sided nuclear magnetic resonance scanner for the in vivo quantification of live cattle marbling. *Appl. Magn. Reson.* **46**, 593–606 (2015)
50. Utsuzawa, S., Tang, Y., Song, Y.-Q.: Inside-out NMR with two concentric ring magnets. *J. Magn. Reson.* **333**, 107082 (2021)
51. Nakashima, Y.: Nondestructive in-site moisture quantification of building materials by single-sided NMR. In: *Proceedings 61st Annual Meeting NMR Society of Japan*, November (2022) [**in Japanese**]
52. Nakashima, Y.: Single-sided multi-ring magnetic circuit. Japanese Patent no 5196480 (2013)
53. Nakashima, Y., Sawatsubashi, T., Fujii, S.: Nondestructive quantification of moisture in powdered low-rank coal by a unilateral nuclear magnetic resonance scanner. *Int. J. Coal Prep. Util.* **42**, 1421–1434 (2022)
54. Himeji City Castle Research Laboratory: *The Fascination of the Slaked Lime Plaster of the Himeji Castle*. Utsumi Printing, Himeji (2017) [**in Japanese**]
55. Nakashima, Y., Shiba, N.: Nondestructive measurement of intramuscular fat content of fresh beef meat by a hand-held magnetic resonance sensor. *Int. J. Food Prop.* **24**, 1722–1736 (2021)
56. Behroozmand, A.A., Keating, K., Auken, E.: A review of the principles and applications of the NMR technique for near-surface characterization. *Surv. Geophys.* **36**, 27–85 (2015)
57. Ishizaki, T., Maruyama, M., Furukawa, Y., et al.: Premelting of ice in porous silica glass. *J. Cryst. Growth.* **163**, 455–460 (1996)
58. Watanabe, K., Mizoguchi, M.: Amount of unfrozen water in frozen porous media saturated with solution. *Cold Reg. Sci. Technol.* **34**, 103–110 (2002)
59. Kose, K. (ed.): *Compact MRI*. Kyoritsu Shuppan Co. Ltd., Tokyo (2004) [**in Japanese**]
60. Blümich, B., Teymouri, Y., Clark, R.: NMR on the road: Non-destructive characterization of the crumb–rubber fraction in asphalt. *Appl. Magn. Reson.* **50**, 497–509 (2019)
61. Jaffel, H., Korb, J.-P., Ndobu-Epoy, J.-P., et al.: Probing microstructure evolution during the hardening of gypsum by proton NMR relaxometry. *J. Phys. Chem. B.* **110**, 7385–7391 (2006)
62. Borgia, G.C., Brown, R.J.S., Fantazzini, P.: Uniform-penalty inversion of multiexponential decay data II. Data spacing,  $T_2$  data, systematic data errors, and diagnostics. *J. Magn. Reson.* **147**, 273–285 (2000)
63. Kowalewski, J., Levy, G.C., Johnson, L.F., et al.: A three-parameter non-linear procedure for fitting inversion-recovery measurements of spin-lattice relaxation times. *J. Magn. Reson.* **26**, 533–536 (1977)
64. Johnson, W., Keller, R.A.: NMR spectroscopic determination of water in deuterium oxide/water mixtures. *Anal. Lett.* **2**, 99–104 (1969)
65. Casieri, C., Senni, L., Romagnoli, M., Santamaria, U., De Luca, F.: Determination of moisture fraction in wood by mobile NMR device. *J. Magn. Reson.* **171**, 364–372 (2004)
66. Livo, K., Saidian, M., Prasad, M.: Effect of paramagnetic mineral content and distribution on nuclear magnetic resonance surface relaxivity in organic-rich Niobrara and Haynesville shales. *Fuel.* **269**, 117417 (2020)
67. Foley, I., Farooqui, S.A., Kleinberg, R.L.: Effect of paramagnetic ions on NMR relaxation of fluids at solid surfaces. *J. Magn. Reson. A.* **123**, 95–104 (1996)
68. Kenyon, W.E., Kolleeny, J.A.: NMR surface relaxometry of calcite with adsorbed  $Mn^{2+}$ . *J. Colloid Interface Sci.* **170**, 502–514 (1995)
69. Anferova, S., Anferov, V., Rata, D.G., et al.: A mobile NMR device for measurements of porosity and pore size distributions of drilled core samples. *Concepts Magn. Reson. B.* **23**, 26–32 (2004)
70. Bray, C.L., Hornak, J.P.: Unilateral MRI using a rastered projection. *J. Magn. Reson.* **188**, 151–159 (2007)

71. Zhang, K., Zhou, J., Yin, Z.: Experimental study on mechanical properties and pore structure deterioration of concrete under freeze-thaw cycles. *Materials*. **14**, 6568 (2021)
72. Nakashima, Y., Kikuchi, T.: Estimation of the apertures of water-saturated fractures by nuclear magnetic resonance well logging. *Geophys. Prospect*. **55**, 235–254 (2007)

**Publisher's Note** Springer Nature remains neutral with regard to jurisdictional claims in published maps and institutional affiliations.